Diffraction-Limited Plenoptic Imaging with Correlated Light

Francesco V. Pepe,[1,*] Francesco Di Lena,[2,1] Aldo Mazzilli,[2] Eitan Edrei,[3] Augusto Garuccio,[2,1,4] Giuliano Scarcelli,[3] and Milena D'Angelo[2,1,4,†]

[1]*INFN, Sezione di Bari, I-70126 Bari, Italy*

[2]*Dipartimento Interateneo di Fisica, Università degli studi di Bari, I-70126 Bari, Italy*

[3]*Fischell Department of Bioengineering, University of Maryland, College Park, Maryland 20742, USA*

[4]*Istituto Nazionale di Ottica (INO-CNR), I-50125 Firenze, Italy*

(Received 4 April 2017; published 15 December 2017)

Traditional optical imaging faces an unavoidable trade-off between resolution and depth of field (DOF). To increase resolution, high numerical apertures (NAs) are needed, but the associated large angular uncertainty results in a limited range of depths that can be put in sharp focus. Plenoptic imaging was introduced a few years ago to remedy this trade-off. To this aim, plenoptic imaging reconstructs the path of light rays from the lens to the sensor. However, the improvement offered by standard plenoptic imaging is practical and not fundamental: The increased DOF leads to a proportional reduction of the resolution well above the diffraction limit imposed by the lens NA. In this Letter, we demonstrate that correlation measurements enable pushing plenoptic imaging to its fundamental limits of both resolution and DOF. Namely, we demonstrate maintaining the imaging resolution at the diffraction limit while increasing the depth of field by a factor of 7. Our results represent the theoretical and experimental basis for the effective development of promising applications of plenoptic imaging.

DOI: 10.1103/PhysRevLett.119.243602

Plenoptic imaging (PI) is a novel optical method for recording visual information [1]. Its peculiarity is the ability to record both the position and propagation direction of light in a single exposure. PI is currently employed in the most diverse applications, from stereoscopy [1–3], to microscopy [4–7], particle image velocimetry [8], particle tracking and sizing [9], wavefront sensing [10–13], and photography, where it currently enables digital cameras with refocusing capabilities [14,15]. The capability of PI to simultaneously acquire multiple-perspective 2D images brings it among the fastest and most promising methods for 3D imaging with available technologies [16]. Indeed, high-speed and large-scale 3D functional imaging of neuronal activity has been demonstrated [7]. Furthermore, the first studies for surgical robotics [17], endoscopic application [18], and blood-flow visualization [19] have been performed.

The key component of standard plenoptic cameras is a microlens array inserted in the native image plane, that reproduces repeated images of the main camera lens on the sensor behind it [1,15]. This enables the reconstruction of light paths, employed, in postprocessing, for refocusing different planes, changing the point of view, and extending the depth of field (DOF) within the acquired image. However, a fundamental trade-off between spatial and angular resolution is naturally built into standard plenoptic imaging. If N_{tot} is the total number of pixels per line on the sensor, N_x the number of microlenses per line, and N_u the number of pixels per line associated with each microlens, then $N_x N_u = N_{\mathrm{tot}}$. Essentially, standard PI gives the same resolution and DOF one would obtain with a N_u times a smaller NA. The final advantage is thus practical rather than fundamental and is limited to a higher luminosity (and hence SNR) of the final image and parallel acquisition of multiperspective images.

Correlation plenoptic imaging (CPI) has recently been proposed for overcoming this fundamental limit [20]. The main idea is to exploit the second-order spatiotemporal correlation properties of light to perform the spatial and directional detection on two distinct sensors: Using correlated beams [20–22], high-resolution "ghost" imaging is performed on one sensor [23–27] while simultaneously obtaining the angular information on the second sensor. As a result, the relation between the spatial (N_x) and the angular (N_u) pixels per line, at fixed N_{tot}, becomes linear: $N_x + N_u = N_{\mathrm{tot}}$ [20].

In this Letter, we present the first experimental realization of CPI. Our CPI scheme has a higher DOF and higher resolution than traditional PI; compared to conventional imaging, it maintains the diffraction-limited resolution but has a 7 times larger DOF. Therefore, CPI truly pushes imaging to the fundamental limits imposed by the wave nature of light. Our proof-of-principle experiment indicates that CPI can enhance the potentials of PI, paving the way towards its promising applications, especially in situations where the fast acquisition typical of PI needs to be accompanied by a high resolution, such as microscopy and 3D imaging. In fact, compared to other 3D imaging techniques, CPI has the advantage of not requiring either scanning methods (as in confocal microscopy), delicate interferometric techniques (as in holography and ptychography), or fast pulsed illumination (as in time-of-flight imaging) [9,28–30].

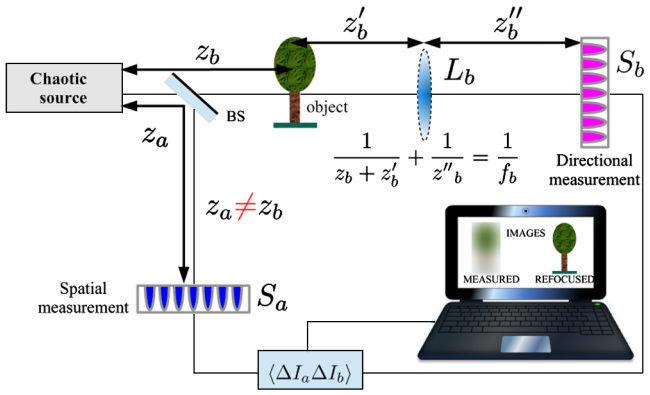

FIG. 1. Schematic representation of the experimental setup employed for correlation plenoptic imaging. The lens L_b replaces the whole microlens array of standard PI.

A schematic representation of the experimental setup is reported in Fig. 1; technical details are in Sec. III of Supplemental Material [31]. Based on the ghost imaging phenomenon [26,27], an intensity correlation measurement between each pixel of S_a and the whole sensor S_b, described by the Glauber correlation function [32], enables retrieving an image of the object on the plane of S_a. Such a ghost image is focused, provided the distance z_a between the source and the sensor S_a is equal to the distance z_b between the source and the object [26,27]: Because of the spatiotemporal correlation properties of chaotic light, the light source plays the role of a focusing element and replaces the lens of a standard imaging system characterized by an image magnification $m = 1$ [27]. This justifies the name of *spatial sensor* for detector S_a, despite it detecting a light beam that has never passed through the object. Like standard imaging, both the maximum achievable resolution set by the diffraction limit (Δx^f) and the DOF of the ghost image are expected to be defined by the numerical aperture of the focusing element (here, the chaotic light source), as seen from the object (NA). In our case, $\Delta x^f = \lambda/\mathrm{NA} = 14\ \mu$m and, for objects at the resolution limit, $\mathrm{DOF} = \lambda/\mathrm{NA}^2 = 0.37$ mm. In our experiment, the pixel size is chosen to be comparable with the maximum achievable resolution: $\delta x = 7.2\ \mu\mathrm{m} \approx \Delta x^f/2$, thus enabling imaging at the diffraction limit.

To understand how CPI enables increasing the DOF of the acquired image and changing the viewpoint (as required for 3D imaging), let us study the role of the high-resolution sensor S_b. Each pixel of this sensor corresponds to the source point from which the detected signal has been emitted. Correlation measurements between pixels of S_a and S_b may thus enable tracing "light rays" by joining each object point with each source point [20,21]. Therefore, the high resolution of S_b does not inhibit the retrieval of the (ghost) image of the object on S_a but simply provides displaced coherent images, one for each source point [see Eq. (8) of Supplemental Material [31]]. The conventional (incoherent) ghost image can be recovered by summing the correlations over the whole sensor S_b, which corresponds to using the typical "bucket" detector of ghost imaging.

The refocusing capability of CPI is governed by the resolution of the source image retrieved by S_b, which is defined, together with the numerical aperture NA_b of the lens L_b, by the diffraction of light at the object (see Sec. I of Supplemental Material [31]) [20,21]. In our experiment, both the resolution limit defined by the lens ($\lambda/\mathrm{NA}_b = 14\ \mu$m) and the pixel size of S_b ($\delta u = 72\ \mu$m) have been chosen in such a way that the resolution on the source plane Δu is mostly defined by the diffraction at the object ($\lambda z_b/a$, where a is the length scale of the smallest details of the object). We thus operate in a regime where imaging performances are limited by the wave nature of light and not by the microlens size as in standard PI.

In our experiment, we have employed a test target to mimic small details and easily monitor the image resolution, both in the out-of-focus and in the refocused image. In Fig. 2, we report the experimental results obtained for element 3 of group 2: The three slits have center-to-center distance $d = 0.198$ mm and slit width $a = d/2$. In the left column, we report the out-of-focus image obtained on S_a by measuring correlation with the whole detector S_b, when the mask is placed significantly out of the focused plane ($z_b - z_a \gtrsim 20$ mm); this is equivalent to the blurred image any conventional imaging system, characterized by the same NA as our CPI scheme, would retrieve at the given defocusing distance. In the right column, we report the same image after implementing the CPI refocusing algorithm [20]

$$\Sigma^{\mathrm{ref}}_{z_a,z_b}(\boldsymbol{\rho}_a) := \int d^2\boldsymbol{\rho}_b \Gamma_{z_a,z_b}\left[\frac{z_a}{z_b}\boldsymbol{\rho}_a - \frac{\boldsymbol{\rho}_b}{M}\left(1-\frac{z_a}{z_b}\right), \boldsymbol{\rho}_b\right], \quad (1)$$

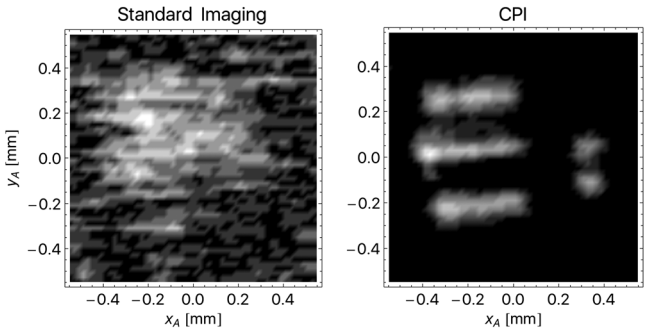

FIG. 2. Comparison between the experimental out-of-focus image obtained by placing the object (element 3 of group 2 of a test target) in $z_b - z_a = 21$ mm (left column) and the corresponding CPI refocused images (right column). This experimental scenario is denoted as measurement B in Fig. 4. The experimental data are taken with a pixel size at the diffraction limit ($\delta x = 7.2\ \mu$m), while the refocused image has a pixel size scaled by a factor of z_b/z_a, in line with Eq. (1) [see also Eq. (12) of Supplemental Material [31]]. After the correlation measurement, low-pass Gaussian filtering and thresholding in the Fourier domain were applied to remove the uncorrelated background.

where $\Gamma_{z_a,z_b}(\boldsymbol{\rho}_a,\boldsymbol{\rho}_b)$ represents the measured correlation of intensity fluctuations $\langle \Delta I_a \Delta I_b \rangle$ between point $\boldsymbol{\rho}_a$ on S_a and point $\boldsymbol{\rho}_b$ on S_b. The refocusing capability of CPI clearly appears from Fig. 2, based on the enhanced resolution and contrast of the refocused image.

To understand the physical origin of the refocusing capability of CPI, we report in Fig. 3(a) the result of the pixel-by-pixel correlation of the intensity fluctuations evaluated on the planes of S_a and S_b [i.e., $\Gamma_{z_a,z_b}(\boldsymbol{\rho}_a,\boldsymbol{\rho}_b)$ from Eq. (15) of Supplemental Material [31], after integration over y_a and y_b], in the same experimental scenario of Fig. 2. For each pixel of the angular sensor S_b, we observe on S_a a displaced image of the object: Hence, imaging the light source on the high-resolution sensor S_b enables changing the perspective on the observed scene [33]. This result explains why the standard ghost image reported in Fig. 3(c) is blurred: When no angular information is retrieved (i.e., when integration over S_b is performed), all displaced images combine into the out-of-focus image $\Sigma_{z_a,z_b}(\boldsymbol{\rho}_a) = \int d^2\boldsymbol{\rho}_b \Gamma_{z_a,z_b}(\boldsymbol{\rho}_a,\boldsymbol{\rho}_b)$. In ghost imaging, integration performed by the bucket detector clearly erases the precious information contained in the raw data of CPI. On the contrary, CPI exploits the extra information gained by the high-resolution detector S_b. As shown in Fig. 3(b), all displaced images are realigned by the reshaping and resizing algorithm that appears in the integrand of Eq. (1); hence, no blurring occurs anymore upon integration over S_b, and the refocused image of Fig. 3(d) is obtained. Figures 3(c) and 3(d) also show excellent agreement between the experimental data (points) and theoretical predictions (solid line).

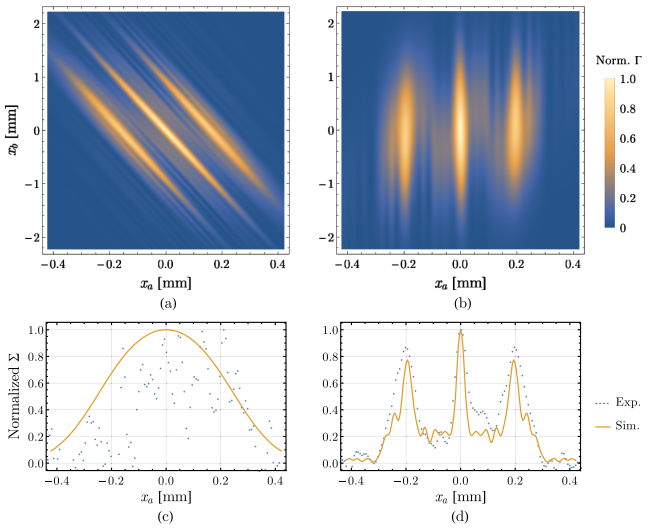

FIG. 3. (a) Simulation of CPI measurements obtained by evaluating the pixel-by-pixel correlation between S_a and S_b in the same scenario employed to get the experimental results of Fig. 2. (b) Result of the refocusing algorithm reported in the integrand of Eq. (1), as applied to the result of panel (a). (c),(d) The solid lines are obtained by integrating the data of panels (a) and (b), respectively, over the angular sensor S_b. (c) coincides with the standard ghost image, while (d) represents the refocused image of CPI, described by Eq. (1). The simulation is based on theoretical predictions reported in Secs. I and II of Supplemental Material [31], after integration over the y direction. Points are experimental data obtained by integrating over y_a the experimental results of Fig. 2.

Let us now focus our attention on the central point of the Letter, namely, the unique opportunity offered by CPI to refocus without sacrificing diffraction-limited image resolution, as defined by the numerical aperture of the imaging system. In Fig. 4(c), the dashed (white) line represents a geometrical-optics prediction for the maximum range of "perfect" refocusing in CPI, given by [20]

$$\left|1-\frac{z_a}{z_b}\right| < \frac{\Delta x}{\Delta u} = \frac{dz_a/z_b}{\max[\lambda z_b/a, 2\lambda/(M_b \mathrm{NA}_b), 2\delta u/M]} \qquad (2)$$

with Δx the resolution on sensor S_a and Δu the resolution on the source plane. In the right-hand side of Eq. (2), we have expressed both quantities in the simple case of double-slit objects of width a and center-to-center distance $d = 2a$. The resolution $\Delta x = dz_a/z_b$ is defined by the geometrical projection of the image of the mask on the sensor plane. The resolution Δu is defined by the larger contribution associated with the diffraction at the object (i.e., $\lambda z_b/a$), the numerical aperture of L_b, and pixel size δu; these last two contributions enter into play for objects quite close to the light source [i.e., for $z_b = 2a/(M_b \mathrm{NA}_b)$ and $z_b = 2\delta u a/(M\lambda)$, respectively]. Based on Eq. (2), the physical quantities defining the spatial and the angular resolution of CPI are thus the object position z_b and the object features a and d. The density plot in Fig. 4(c) reports visibility $V(d/\Delta x^f, z_b - z_a)$ of the refocused CPI images of double-slit masks, evaluated in the present experimental setup

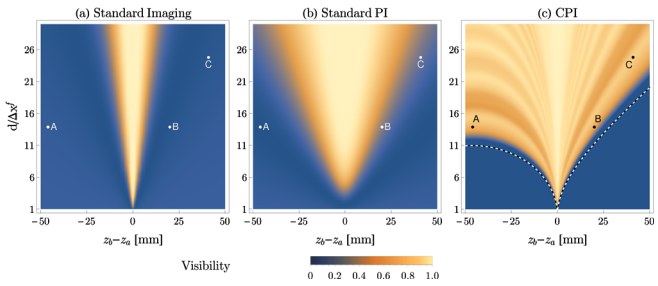

FIG. 4. Analysis of the range of perfect refocusing for double-slit objects with $d = 2a$; the slit distance d is normalized to the resolution of the focused image Δx^f. Visibility is computed by considering (a) standard imaging, (b) standard plenoptic imaging (with $N_u = 3$), and (c) CPI devices sharing the same NA employed in the experiment. Points A, B, and C correspond to the experimental scenarios leading to the results reported in Fig. 2 above and Figs. S2(a) and S2(b) of Supplemental Material [31]; the (white) dashed line in (c) is the geometrical perfect refocusing limit given by Eq. (2).

(see Secs. I and II of Supplemental Material [31]). Besides giving the degree of reliability of the geometrical prediction of Eq. (2), this plot unveils the physical limit of the resolution and DOF in CPI [34].

To compare CPI with both standard imaging and standard PI, we consider imaging devices having the same NA as the light source in our experiment and report in Figs. 4(a) and 4(b) the visibility they achieve [35]. For standard PI, we have considered $N_u = 3$ to avoid strongly compromising the image resolution. A comparison of Figs. 4(a), 4(b), and 4(c) indicates that CPI combines at best the advantages of standard and plenoptic imaging: It preserves the resolution of standard imaging while increasing the DOF even beyond typical values of standard PI. Interestingly, close up ($z_b < z_a$), object details larger than $d \gtrsim \sqrt{8\lambda z_a} \simeq 2.8\Delta x^f$ (the refocusing limit corresponding to $z_b = z_a/2$) can always be refocused by CPI, no matter how close the object is to the source. For $z_b > z_a$, the maximum achievable depth of field is significantly larger than in both standard imaging and standard PI. As demonstrated in Sec. IV of Supplemental Material [31] (see Figs. S4 and S5 therein), the refocusing range in CPI is limited by the interference and diffraction at the object, for close up, and only by diffraction, for distant objects. Such a dependence can be understood in terms of the Klyshko picture [36], as applied to ghost imaging with chaotic light [26]. Hence, CPI reaches the fundamental limits imposed by the wave nature of light to both the image resolution and DOF.

Points A, B, and C in Fig. 4 represent the experimental scenarios corresponding to the results reported in Fig. 2 (B) and in Figs. S2(a) and S2(b) of Supplemental Material [31] (A and C). In all three points, CPI clearly guarantees a significant DOF advantage. In particular, the object corresponding to A and B can be refocused by CPI in a range more than 7 times larger than in standard imaging and 2.5 larger than in a standard PI device characterized by a 3 times worse spatial resolution ($N_u = 3$). For the wider object corresponding to point C, the maximum achievable DOF with CPI is 4 times larger than with standard imaging and twice larger than with a standard PI with $N_u = 3$. It is worth emphasizing that the DOF of the standard ghost image represents the axial resolution of CPI ($\Delta z^{\mathrm{CPI}} = \lambda/\mathrm{NA}^2$); hence, the ratio between the depth of fields of CPI and standard imaging fixes the number of planes that can be refocused by CPI.

To summarize the above results, in Fig. 5, we plot the DOF enhancement offered by CPI with respect to standard PI as a function of the resolution compromise of conventional PI. The DOF enhancement is defined as the ratio between the maximum achievable DOF of CPI and standard PI; the resolution compromise of standard PI corresponds to the ratio between the maximum image resolutions of standard PI and CPI or standard imaging and is represented by the number of angular pixels N_u of

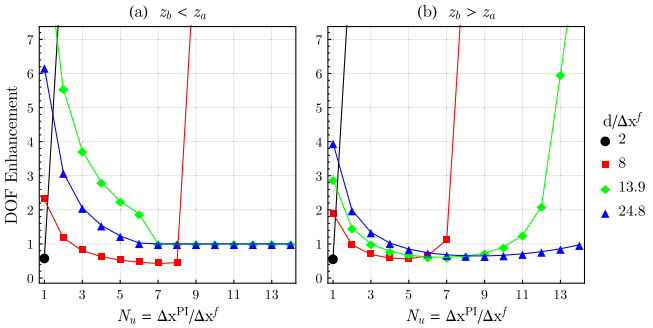

FIG. 5. Comparison between standard PI and CPI in terms of the maximum achievable DOF versus resolution. The comparison is made for double-slit masks of varying distance d and width $a = d/2$. DOFs are evaluated by considering the maximum (z_b^M) and minimum (z_b^m) values of the object distance for which the image is still resolved based on the Rayleigh criterion (namely, $V \geq 10\%$). We report the results for (a) $z_b < z_a$ and (b) $z_b > z_a$ obtained by considering the present experimental setup for CPI and an equivalent standard PI device.

standard PI. All parameters are the same employed in Fig. 4. To better emphasize the lack of a refocusing limit for close up, we have chosen to separately plot the two cases of an object closer to and farther away from the conjugate plane $z_b = z_a$. In line with the results in Fig. 4, CPI always outperforms standard PI. In fact, the DOF of CPI is generally larger than for standard PI, although there are ranges of N_u where PI may overcome the DOF of CPI by losing resolution.

Conclusions and outlook.—We have demonstrated that CPI can push plenoptic imaging to its fundamental limits of both the resolution and maximum achievable DOF: Unlike standard PI, CPI has no constraints on image resolution, which stays diffraction limited as in standard imaging systems. Still, CPI enables increasing the DOF well beyond the typical value of standard imaging. The advantages of both standard and plenoptic imaging are thus combined at best in CPI, whose maximum achievable DOF is solely limited by the interference and diffraction at the object (see, e.g., Figs. S4 and S5 of Supplemental Material [31]). Several technologies have been introduced in the past years where light correlation properties enable going beyond the capabilities of standard imaging systems (e.g., [23,26,37–40]); however, in most cases, previous technologies exploited the correlations in either the position or momentum but not both. The simultaneous use of both momentum and position correlation has so far been used only for fundamental demonstrations [41–43]; here, for the first time, it is exploited to push the fundamental limits of practical imaging systems.

CPI has the potential to strongly improve the performances of both microscopy, where high lateral and axial resolutions are required together with a large DOF, and 3D imaging, where fast multiperspective acquisitions are

desired. Future studies will be devoted to acquisition time optimization, considering hardware (fast CMOS, smart sensors [44]) and software solutions (compressed-sensing and sparse measurement techniques [45]) to regain the single-shot advantage of conventional plenoptic imaging.

The authors thank T. Macchia, C. Plantamura, and C. Bevilacqua for participating in the preliminary experimental activity. M. D. acknowledges financial support from the Italian Ministry of Education, University and Research (MIUR), Project No. PONa3_00369 ("Laboratorio per lo Sviluppo Integrato delle Scienze e delle Tecnologie dei Materiali Avanzati e per dispositivi innovativi-LABORATORIO SISTEMA"). M. D., F. D., A. M., and A. G. acknowledge financial support from MIUR, Project No. PON02-00576-3333585 (P. O. N. RICERCA E COMPETITIVITÀ 2007-2013—Avviso No. 713/Ric. del 29/10/2010, Titolo II—"Sviluppo/Potenziamento di DAT e di LPP"). M. D., F. D., A. G., and F. V. P. are partially supported by Istituto Nazionale di Fisica Nucleare (INFN) through the projects "QUANTUM" and "PICS."

*francesco.pepe@ba.infn.it
†milena.dangelo@uniba.it

[1] E. H. Adelson and J. Y. Wang, Single lens stereo with a plenoptic camera, IEEE Trans. Pattern Anal. Mach. Intell. **14**, 99 (1992).
[2] S. Muenzel and J. W. Fleischer, Enhancing layered 3d displays with a lens, Appl. Opt. **52**, D97 (2013).
[3] M. Levoy and P. Hanrahan, in *Proceedings of the 23rd Annual Conference on Computer Graphics and Interactive Techniques* (Association for Computing Machinery, New York, 1996), pp. 31–42.
[4] M. Levoy, R. Ng, A. Adams, M. Footer, and M. Horowitz, Light field microscopy, ACM Trans. Graph. **25**, 924 (2006).
[5] M. Broxton, L. Grosenick, S. Yang, N. Cohen, A. Andalman, K. Deisseroth, and M. Levoy, Wave optics theory and 3-d deconvolution for the light field microscope, Opt. Express **21**, 25418 (2013).
[6] W. Glastre, O. Hugon, O. Jacquin, H. G. de Chatellus, and E. Lacot, Demonstration of a plenoptic microscope based on laser optical feedback imaging, Opt. Express **21**, 7294 (2013).
[7] R. Prevedel, Y.-G. Yoon, M. Hoffmann, N. Pak, G. Wetzstein, S. Kato, T. Schrödel, R. Raskar, M. Zimmer, E. S. Boyden, and A. Vaziri, Simultaneous whole-animal 3d imaging of neuronal activity using light-field microscopy, Nat. Methods **11**, 727 (2014).
[8] T. W. Fahringer, K. P. Lynch, and B. S. Thurow, Volumetric particle image velocimetry with a single plenoptic camera, Meas. Sci. Technol. **26**, 115201 (2015).
[9] E. M. Hall, B. S. Thurow, and D. R. Guildenbecher, Comparison of three-dimensional particle tracking and sizing using plenoptic imaging and digital in-line holography, Appl. Opt. **55**, 6410 (2016).
[10] C. W. Wu, Ph.D. thesis, University of Maryland, College Park, 2016.
[11] Y. Lv, R. Wang, H. Ma, X. Zhang, Y. Ning, and X. Xu, SU-G-IeP4-09: Method of human eye aberration measurement using plenoptic camera over large field of view, Med. Phys. **43**, 3679 (2016).
[12] C. Wu, J. Ko, and C. C. Davis, Using a plenoptic sensor to reconstruct vortex phase structures, Opt. Lett. **41**, 3169 (2016).
[13] C. Wu, J. Ko, and C. C. Davis, Imaging through strong turbulence with a light field approach, Opt. Express **24**, 11975 (2016).
[14] https://www.lytro.com/illum, http://www.raytrix.de/.
[15] R. Ng, M. Levoy, M. Brédif, G. Duval, M. Horowitz, and P. Hanrahan, Stanford University Computer Science Tech Report CSTR 2005-02, 2005.
[16] X. Xiao, B. Javidi, M. Martinez-Corral, and A. Stern, Advances in three-dimensional integral imaging: Sensing, display, and applications, Appl. Opt. **52**, 546 (2013).
[17] A. Shademan, R. S. Decker, J. Opfermann, S. Leonard, P. C. Kim, and A. Krieger, in *Proceedings of the 2016 IEEE International Conference on Robotics and Automation (ICRA)* (IEEE, New York, 2016), pp. 708–714.
[18] H. N. Le, R. Decker, J. Opferman, P. Kim, A. Krieger, and J. U. Kang, in *CLEO: Applications and Technology* (Optical Society of America, Washington, DC, 2016), paper AW4O.2.
[19] M. F. Carlsohn, A. Kemmling, A. Petersen, and L. Wietzke, in *SPIE Photonics Europe* (International Society for Optics and Photonics, Cardiff, 2016), p. 989703.
[20] M. D'Angelo, F. V. Pepe, A. Garuccio, and G. Scarcelli, Correlation Plenoptic Imaging, Phys. Rev. Lett. **116**, 223602 (2016).
[21] F. V. Pepe, G. Scarcelli, A. Garuccio, and M. D'Angelo, Plenoptic imaging with second-order correlations of light, Quantum Meas. Quantum Metrol. **3**, 20 (2016).
[22] F. V. Pepe, F. Di Lena, A. Garuccio, G. Scarcelli, and M. D'Angelo, Correlation plenoptic imaging with entangled photons, Technologies—Open Access Multidisciplinary Engineering Journal **4**, 17 (2016).
[23] T. B. Pittman, Y. H. Shih, D. V. Strekalov, and A. V. Sergienko, Optical imaging by means of two-photon quantum entanglement, Phys. Rev. A **52**, R3429 (1995).
[24] A. Gatti, E. Brambilla, M. Bache, and L. A. Lugiato, Ghost Imaging with Thermal Light: Comparing Entanglement and Classical Correlation, Phys. Rev. Lett. **93**, 093602 (2004).
[25] M. D'Angelo and Y. Shih, Quantum imaging, Laser Phys. Lett. **2**, 567 (2005).
[26] A. Valencia, G. Scarcelli, M. D'Angelo, and Y. Shih, Two-Photon Imaging with Thermal Light, Phys. Rev. Lett. **94**, 063601 (2005).
[27] G. Scarcelli, V. Berardi, and Y. Shih, Can Two-Photon Correlation of Chaotic Light Be Considered as Correlation of Intensity Fluctuations?, Phys. Rev. Lett. **96**, 063602 (2006).
[28] J. Mertz, *Introduction to Optical Microscopy* (Roberts and Company, Englewood, CO, 2009).
[29] M. K. Kim, Principles and techniques of digital holographic microscopy, SPIE Rev. **1**, 018005 (2010).
[30] M. Hansard, S. Lee, O. Choi, and R. Horaud, *Time of Flight Cameras: Principles, Methods, and Applications* (Springer, Berlin, 2013).

[31] See Supplemental Material at http://link.aps.org/supplemental/10.1103/PhysRevLett.119.243602 for (i) the analytical computation leading to Eq. (1) and to the evaluation of resolutions, (ii) a detailed description of the experimental setup and parameters, (iii) the experimental results for points A and C in Fig. 4, and (iv) the description of the procedure to determine the DOF advantage of CPI.

[32] M. O. Scully and M. S. Zubairy, *Quantum Optics* (Cambridge University Press, Cambridge, England, 1997).

[33] The change of viewpoint is a common feature of both PI and CPI, with the only difference that, in CPI, it is obtained with a single lens (L_b) rather than by the microlens array typical of standard PI, and it is thus significantly larger. Despite the fact that we do not use it in the present work, it is worth emphasizing the key role played by the change of perspective and its achievable resolution, for implementing 3D imaging.

[34] The slight oscillations appearing in the density plot come from the intrinsically coherent nature of CPI.

[35] In these cases, the defocusing distance $z_b - z_a$ represents the distance of the object (placed in z_b) from the exact conjugate object plane (namely, $z_a = s_o$ satisfies the thin lens equation $1/s_o + 1/s_i = 1/f$, where s_i is the distance of the lens from the image and f is the lens focal length).

[36] D. N. Klyshko, Effect of focusing on photon correlation in parametric light scattering, Sov. Phys. JETP **67**, 1131 (1988).

[37] O. Schwartz, J. M. Levitt, R. Tenne, S. Itzhakov, Z. Deutsch, and D. Oron, Superresolution microscopy with quantum emitters, Nano Lett. **13**, 5832 (2013).

[38] Y. Israel, R. Tenne, D. Oron, and Y. Silberberg, Quantum correlation enhanced super-resolution localization microscopy enabled by a fibre bundle camera, Nat. Commun. **8**, 14786 (2017).

[39] T. Dertinger, R. Colyer, G. Iyer, S. Weiss, and J. Enderlein, Fast, background-free, 3D super-resolution optical fluctuation imaging (SOFI), Proc. Natl. Acad. Sci. U.S.A. **106**, 22287 (2009).

[40] G. Barreto Lemos, V. Borish, G. D. Cole, S. Ramelow, R. Lapkiewicz, and A. Zeilinger, Quantum imaging with undetected photons, Nature (London) **512**, 409 (2014).

[41] R. S. Bennink, S. J. Bentley, R. W. Boyd, and J. C. Howell, Quantum and Classical Coincidence Imaging, Phys. Rev. Lett. **92**, 033601 (2004).

[42] M. D'Angelo, Y. H. Kim, S. P. Kulik, and Y. Shih, Identifying Entanglement Using Quantum Ghost Interference and Imaging, Phys. Rev. Lett. **92**, 233601 (2004).

[43] G. Scarcelli, Y. Zhou, and Y. Shih, Random delayed-choice quantum eraser via two-photon imaging, Eur. Phys. J. D **44**, 167 (2007).

[44] *TOF Range-Imaging Cameras*, edited by F. Remondino and D. Stoppa (Springer, Berlin, 2013).

[45] O. Katz, Y. Bromberg, and Y. Silberberg, Compressive ghost imaging, Appl. Phys. Lett. **95**, 131110 (2009).